Simulation of thermal stresses in anode-supported solid oxide fuel cell stacks. Part II: Loss of gas-tightness, electrical contact and thermal buckling

Arata Nakajo*, Zacharie Wuillemin, Jan Van herle, Daniel Favrat

Laboratoire d'Energétique Industrielle (LENI), Institut de Génie Mécanique, Ecole Polytechnique Fédérale de Lausanne, 1015 Lausanne, Switzerland

ARTICLE INFO

ABSTRACT

Structural stability issues in planar solid oxide fuel cells arise from the mismatch between the coefficients of thermal expansion of the components. The stress state at operating temperature is the superposition of several contributions, which differ depending on the component. First, the cells accumulate residual stresses due to the sintering phase during the manufacturing process. Further, the load applied during assembly of the stack to ensure electric contact and flatten the cells prevents a completely stress-free expansion of each component during the heat-up. Finally, thermal gradients cause additional stresses in operation.

The temperature profile generated by a thermo-electrochemical model implemented in an equation-oriented process modelling tool (gPROMS) was imported into finite-element software (ABAQUS) to calculate the distribution of stress and contact pressure on all components of a standard solid oxide fuel cell repeat unit.

The different layers of the cell in exception of the cathode, i.e. anode, electrolyte and compensating layer were considered in the analysis to account for the cell curvature. Both steady-state and dynamic simulations were performed, with an emphasis on the cycling of the electrical load. The study includes two different types of cell, operation under both thermal partial oxidation and internal steam–methane reforming and two different initial thicknesses of the air and fuel compressive sealing gaskets.

The results generated by the models are presented in two papers: Part I focuses on cell cracking. In the present paper, Part II, the occurrences of loss of gas-tightness in the compressive gaskets and/or electrical contact in the gas diffusion layer were identified. In addition, the dependence on temperature of both coefficients of thermal expansion and Young's modulus of the metallic interconnect (MIC) were implemented in the finite-element model to compute the plastic deformation, while the possibilities of thermal buckling were analysed in a dedicated and separate model.

The value of the minimum stable thickness of the MIC is large, even though significantly affected by the operating conditions. This phenomenon prevents any unconsidered decrease of the thickness to reduce the thermal inertia of the stack. Thermal gradients and the shape of the temperature profile during operation induce significant decreases of the contact pressure on the gaskets near the fuel manifold, at the inlet or outlet, depending on the flow configuration. On the contrary, the electrical contact was ensured independently of the operating point and history, even though plastic strain developed in the gas diffusion layer.

1. Introduction

The solid oxide fuel cell (SOFC) is a direct energy conversion device, which allows the production of electricity with high efficiency while maintaining pollutant emissions at a low level. Prototypes have successfully proven their ability to achieve these aims. However, the SOFC technology faces many challenges when it comes to commercialisation, since costs reductions and extended lifetime are required. Under steady-state operation, failures of the SOFC stack arise from the degradation of the materials, which is induced by the high temperature and aggressive environment. In addition, in a system in operation, failure of auxiliary components can cause harmful conditions on the SOFC stack such as a reduction–oxidation (redox) cycle, which is a well-known cause of failure or strong degradation of the cell performance in the best case [1,2].

The SOFC field is characterised by a strong coupling of the phenomena. The efforts to increase the reliability of SOFC components cover overlapping research fields. In particular, mechanical issues

* Corresponding author.
E-mail addresses: arata.nakajo@epfl.ch (A. Nakajo), zacharie.wuillemin@epfl.ch (Z. Wuillemin), jan.vanherle@epfl.ch (J. Van herle), daniel.favrat@epfl.ch (D. Favrat).

Nomenclature

Symbols

C	Constant
E	young modulus [Pa]
Y	yield limit [Pa]

Greek letters

ν	Poisson ratio
ρ	density [kg m^{-3}]

Indices

el	elastic
Th	thermal

Superscripts

*	porous state
GDL	gas diffusion layer

Acronyms

GDL	gas diffusion layer
INI	analysis steps during initialisation of the contact simulations
IV	analysis steps during current–voltage characterisation
LS	analysis steps during the variation of the electrical load
MIC	metallic interconnect
RT	room temperature
SH	analysis steps during the rapid electrical load shutdown and cooldown
SMR	steam–methane reforming
TPOX	thermal partial oxidation

will affect the thermo-electrochemical behaviour of a planar SOFC stack, through for instance local loss of electrical contact or gas-tightness. These issues may themselves arise from the modification of the temperature profile induced by the degradation of the cell performance. As a consequence, experiments usually end up by the mechanical failure of one of the components. Typical mechanical issues of interest are cell fracture, loss of gas-tightness of the gas compartments and buckling and plastic deformation of the metallic interconnects (MICs).

There are several causes of stresses in a cell. First, the sintering phase during the manufacturing process induces residual stresses due to the mismatch between the coefficients of thermal expansion (CTE) of the materials of the cell. Therefore, the mechanical load applied during the assembly of the stack has to account for the curvature of the cell in order to ensure both the electrical contact and the gas-tightness of the compartments if compressive seals are used. Then, once loaded, friction prevents a stress-free expansion of each component during heat-up and operation. The last manufacturing step of a SOFC stack is usually the reduction procedure of the anode, which takes place when the fuel is fed for the first time. The mechanical properties of the anode support change and influence the cell curvature. Thus the stresses in a stack after a thermal cycle and after the assembly are expected to be different. Finally, the temperature profile during operation causes additional stresses in all layers of the repeat unit. The features of the temperature profile during operation obviously depend on the stack design as well as on the control strategy, flow configuration and fuel composition. Zones of relatively high temperature may induce buckling and will cause a redistribution of the assembly load, which might lead to a partial loss of electrical contact and applied pressure on the gas-

kets. The latter phenomena can also arise from the CTE mismatch of adjacent components, typically gasket and gas diffusion layer (GDL), if the assembly load is not sufficient. Hence, the temperature profile has to be known with accuracy and the reliability of the thermo-electrochemical model is paramount.

Only few studies have been carried out on stresses in SOFC. Yakabe et al. [3,4] were among the first to address both the thermal and chemical stress issues, by coupling thermo-electrochemical models with structural analysis. Experimental work using the X-ray diffraction method was carried out to compare the computed and actual residual stresses in the electrolyte of an anode-supported cell [5,6]. Selimovic et al. [7] considered the effect of the choice of either metallic or ceramic interconnects on the stresses through the differences in computed temperature profiles, during operation, heat-up and shutdown procedures. Lin et al. [8] developed a finite-element model of a 5-cell stack meshed with linear shell elements, which included all components of their SOFC stacks. Plastic deformation was considered. The probability of survival was monitored during transient operation for tubular SOFC [9]. Nevertheless, most studies on standard repeat units (SRU) or stacks did not consider the effect of the residual stress, i.e. stress state and change of curvature of the cell, thermal buckling nor loss of either electrical contact or gas-tightness.

The data on mechanical properties of the relevant component is currently increasing but remains sparse, in particular when the temperature dependence is regarded. The 2-parameter Weibull analysis is widely accepted to characterise the ceramic components [10–12]. Some key parameters are still difficult to find in literature, due to the difficulty in manufacturing or testing. A typical example is the properties of the reduced anode material at high temperature due to the need of a reducing atmosphere above approximately 673 K. The cathode materials are studied extensively in dense state [13,14], but very little information on the properties of porous cathode is available [11]. Engineering data on the properties of alloys used as MIC material is available [15], even though detailed constitutive models could not be found. Metallic foams can be used as GDL. Extensive research has been carried out in the field, even though not specifically on SOFC materials [16]. The mechanical behaviour of compressive sealant materials used as gaskets for SOFC is complex and has not been studied extensively, even though their performance, measured as a leak flux has been estimated. [17–19] showed that their compressive behaviour follows non-linear and differentiated loading and unloading paths, together with plasticity. The properties were found to change significantly during the first loading cycles. Creep at high temperature was observed as well.

Thermo-electrochemical models are more common, and are based on the knowledge acquired with micro-modelling of electrodes [20–22]. Studies underscored the need for refined models with dynamic capabilities to simulate the conditions a real stack will have to face during operation [23].

The framework of the present study is the FP6 European project FLAMESOFC, which aims at developing a cogeneration system foreseen for domestic application. A particular feature of the project is the thermal partial oxidation (TPOX) reformer. The 2.5 kWe class stack design was developed at LENI-EPFL, in collaboration with HTceramix-SOFCPower. The manifold of the stack is external and can accommodate both co- and counter-flow configurations. The active area is 198.5 cm^2.

The aim of the present work is to study the mechanical issues in a standard SOFC repeat unit with an anode-supported cell during the typical phases of its service, i.e. assembly, heat-up, current–voltage (IV) characterisation, dynamic operation, load shutdown and cool-down. The approach consists in importing into finite-element software the temperature profile computed by a reasonably detailed and experimentally calibrated thermo-electrochemical model of a SRU with dynamic capabilities. The

results are presented in two papers: the present one (Part II) explores the issues related to the compressive seal gaskets, to the GDL and to the MIC, i.e. loss of gas-tightness and/or electrical contact, plastic deformation and thermal buckling of the interconnect, while Part I [24] focused on the description of the modelling approach, including the thermo-electrochemical model and the computation of the probability of failure of the cells. First, a simple dedicated model is used to assess the occurrence of thermal buckling of the MIC, depending on the operating conditions. Then, emphasis is placed on the interaction between the components, through contact simulations. Here, the previously computed minimum stable thickness of the MIC is a prerequisite condition. The contact simulations provide information on the distribution and evolution of applied pressure on the gaskets and the GDLs. Particular attention is paid to the choice of the material properties, by considering the temperature dependence when data is available. Plastic deformation of the MIC and the GDL are implemented in the model, while the constitutive law for the compressive gaskets includes non-linear, differentiated loading and unloading paths.

2. Modelling

2.1. Thermo-electrochemical model

The capabilities of an existing thermo-electrochemical model described by Larrain et al. [25] were extended. The equations were implemented in gPROMS, an equation-oriented process-modelling tool [26]. Model evolutions include the adaptation of the geometry to the FLAMESOFC stack, the modifications of the conservation of species to handle internal steam-methane reforming, the implementation of proportional integral derivative (PID) controllers and an in-depth revision of the electrochemical model. The geometry and components of the SRU are depicted in Fig. 1.

An extensive description of the model has been provided in Part I [24]. Thus, the main features are only briefly listed hereafter:

Fig. 1. Top: geometry and components of the standard repeat unit, indicated flow direction holds for co-flow configuration. Location A and B refers to either air inlet or outlet and correspond to points of interest, used for the monitoring of the evolution of the contact status on the gaskets. Bottom: overview of the contributions considered in the electrochemical model at the cell level.

- The SRU is spatially discretised in the in-plane direction and coupled to a local one-dimensional electrochemical model, which is discretised through the thickness of the cell.
- The model is not fully dynamic in terms of species transport and heat transfer, since only thermal inertia of the solid structure is accounted for.
- Boundary conditions include the heat losses to the environment through the insulation. Heat exchange by radiation between the stack and its surrounding is modelled in a simplified manner, i.e. each node is coupled to an equivalent front node of the insulation. The exchange with above/underneath and front/rear nodes is neglected [27].
- The species on the fuel side are restricted to H_2, H_2O, CO, CO_2, CH_4 and N_2.
- The conservation of energy of gases as well as the conservation of species accounts for variations of gas densities.
- The gas velocity is described by the common Darcy law, which is solved along with the mass conservation.

The core of the model is the electrochemical model. It considers both ohmic and non-ohmic losses (see insert in Fig. 1):

- Ohmic losses include the ionic resistance of the electrolyte [28], affected by current constriction in the case of thin layers [29], the electrical resistance of the MIC and a small electronic conductivity of the electrolyte, which induces a small leakage current [25].
- On the anode side, the dusty-gas model [30] is solved in one-dimension through the anode support, along with the equation of continuity. The water–gas-shift reaction is assumed at equilibrium until the interface between the anode and the electrolyte, whereas steam–methane reforming is computed according to the kinetic approach of Achenbach [31]. Currently only hydrogen is electrochemically converted at the interface, according to the relation from Bessler [32].
- On the cathode side, a model of mixed-ionic and electronic conductor solves the charge balance along with the mass transport [20–22]. The coupling between both systems is performed by the transfer current, which is described following the approach of van Heuveln [33].

Finally, three PIDs control (i) the air outlet temperature by the air flow, (ii) the cell potential by the fuel flow and (iii) the electrical power by the current density. Here, the aim is not to propose an efficient control strategy, but rather to identify possible harmful conditions that can be induced by a simple and unrefined control.

2.2. Mechanical model

2.2.1. Assessment of thermal buckling

The temperature profiles generated by the thermo-electrochemical model are imported in a model of an isolated MIC implemented in ABAQUS [34], a numerical tool based on the finite-element method. The mesh was made of second-order, reduced-integration elements (C3D20R) and geometric non-linearity is enabled. The analysis proceeds in two steps. First, the temperature profile is applied in conjunction with a small-distributed pressure of the same shape as the temperature profile. Then, the load is released and the final shape qualitatively observed to identify a possible risk of buckling, in which case the MIC is not flat at the end of the final step. Only elastic deformation is considered to prevent any bias in the results that might be caused by plastic deformation generated during the perturbation step.

2.2.2. Model of standard repeat unit for contact simulations

The uncoupled linear thermo-elastic theory is used for the computation of the stresses. The three-dimensional computer-aided
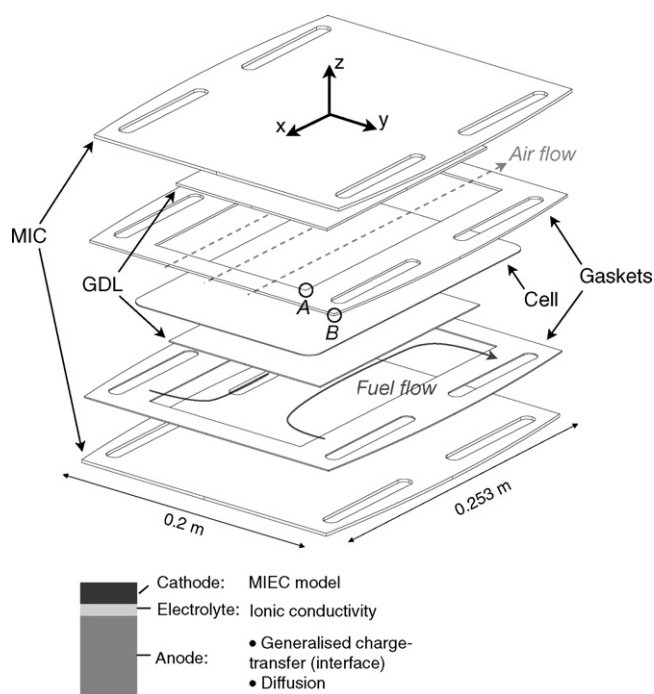
design (CAD) drawings were imported, assembled and meshed in ABAQUS. Three-dimensional reduced linear (C3D8R) and second-order elements (C3D20R) are used in combination to second-order (S8R) shell elements and linear gasket elements (GK3D8R). The contact algorithm of ABAQUS is used to compute the interaction between the components.

A detailed description of the model has been provided in Part I [24]. Thus, the main assumptions of interest for the present part are briefly listed hereafter.

- Small deformations,
- Small-sliding, surface-to-surface, softened contact is assumed between all components. A default value of 0.2 was used for the friction coefficient for the tangential behaviour of all interactions.
- The choice of 2.5 mm-thick MICs prevents any thermal buckling. Thus the middle plane through the thickness of each MIC is constrained to remain flat, whereas rotations around only the *y*-axis (see Fig. 1) are allowed. Therefore, the computations are performed for only one half of a repeat unit.
- The assembly load of 5000 N is transmitted to the SRU by an analytical rigid surface. This value was kept constant for the present study, even though it can be easily varied.
- The cathode is neglected in the contact simulations due to memory limitations, since it has the lowest Young modulus, hence the lowest influence on the cell curvature.

All pre- and post-processing tasks are preformed by MATLAB [35] routines. They are required to (i) import the temperature profile computed by gPROMS, which is performed for each in-plane layers of the ABAQUS mesh and the set of mechanical properties (ii) handle the ABAQUS analysis restarts. Such approach is required when plastic deformation is considered, due to the dependence on the operation history. Moreover, mechanical loading, heat-up and reduction steps have to be simulated prior to operation. This initialisation sequence starts first, by the sintering phase, which is handled by setting artificial CTEs in the electrolyte, compensating layer [36] and cathode combined to an increase of temperature of 1 K (Part I [24]). Then, an additional initialisation step is added to account for the possible variation of the initial thickness of the gaskets relative to the GDL to control the distribution of the assembly load: an anisotropic and artificial thermal strain is induced in the gaskets prior to the assembly, in a similar manner to the sintering step. Finally, the mechanical properties of the anode support are modified during the reduction step. A uniform value of 1073 K was used for all computations of the reduction process within this work. The required parameters are listed in Table 1.

Compressive gaskets usually have a complex behaviour, as shown in Fig. 2, where the applied pressure is plotted against the closure, i.e. the effective strain $\varepsilon - \varepsilon_{Th}$. Gaskets elements embedded in ABAQUS uncouple the in-plane and through-the-thickness behaviour. Non-linear, differentiated loading and unloading path together with plasticity is considered for the latter. The full pattern depicted in the bottom plot of Fig. 2 is required for the simulation of the contact interactions in a stack [18]: the information provided by Bram et al. [17], which consists in the evolution of the gasket behaviour during cyclic loading between no stress and 1.44 MPa is not sufficient for the present study. Therefore, the full pattern (Fig. 2, top) was used, and the value of the closure at maximum pressure adapted according to the data from Bram et al. [17].

Engineering stress–strain curves from alloy suppliers [15] were implemented in the model. GDLs made of metallic foam were considered. Their properties were estimated by the relations proposed by Gibson et al. [16] from the ones of the dense materials [15,41]:

$$\frac{Y_{el}^*}{E_s} \approx 0.05 \left(\frac{\rho^*}{\rho_s}\right)^2 \tag{25}$$
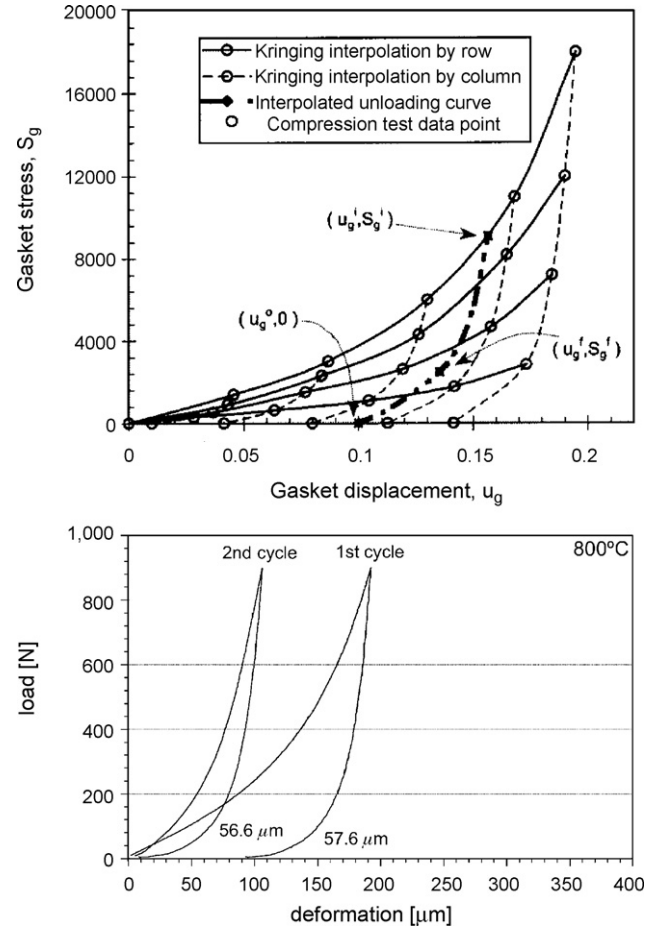

Fig. 2. Typical behaviour of gaskets under compressive loading from [18] (top) and [17] (bottom).

$$\frac{E^*}{E_s} \approx C_1 \left(\frac{\rho^*}{\rho_s}\right)^2, \quad \frac{G^*}{E_s} \approx C_2 \left(\frac{\rho^*}{\rho_s}\right)^2 \tag{26}$$

$$\upsilon^* \approx \frac{C_1}{2C_2} - 1 \tag{27}$$

2.3. Investigated cases

The same sets of cases investigated in Part I [24] are considered for the present study. The analysis of the evolution of the contact pressure on the GDLs and gaskets were performed for different cell types, flow configurations, fuel fed into the SRU and initial thicknesses of the gaskets.

Cell suppliers propose different types of anode-supported cells made of different materials. The curvature of the cell, hence contact status at the interfaces of the components is of interest for the present study and depends for a fixed anode support on (i) the choice of the cathode and associated compatibility layer and (ii) presence of an anode compensating layer, sometimes added to limit the cell curvature and allow an easier and more precise assembly [36]. Two different types of cell were considered for the structural analysis:

- C1: anode, electrolyte, LSM cathode.
- C2: compensating layer, anode, electrolyte, LSM cathode.

Their thickness and mechanical properties are listed in Table 1. The electrochemical performance of C1 and C2 differs from the anode-supported cell with LSCF cathode, on which the electro-

Table 1
Mechanical properties of the components of the standard repeat unit from [5–13,15–17,19,37–41].

		Porosity [%]	Layer thickness [m]	Reduction strain [%]	Zero stress temperature [K]	Young's modulus [GPa]	Poisson's coefficient	Coefficient of thermal expansion $*10^{-6}$ [K^{-1}]	Elastic limit [MPa]	Characteristic strength [MPa]	Weibull modulus
Cathode (LSM)	RT	0.36	35e−6	–	1323[a]	29.7[b]	0.25	11.7	–	52[b]	6.7[b]
	HT									75[b]	3.7[b]
Electrolyte (YSZ)	RT	0	7e−6	–	1473	215	0.317	10.2[c]	–	232	5.7
	HT					185				154	8.6
Anode (NiO-YSZ)	–	0.17	542e−6	–	1473	131[b]	0.317	12.2[c]	–	97 (86,110)	6.8 (4.3,9.8)
Anode (Ni-YSZ)	–	0.36	542e−6	0.07	1473	69[b]	0.317	12.6[c]	–	79 (73,85)	7 (4.8,10.1)
Compensating layer (YSZ)	RT	0	4e−6	–	1473	215	0.317	10.2[c]	–	232	5.7
	HT					185				154	8.6
GDL anode (Ni)	RT	5w	1e−3	–	–	0.154[d]	0.3	16.2[c]	0.63[d]	–	–
	HT					0.114[d]			0.188[d]		
GDL cathode	RT	5w	2e−3	–	–	0.147[d]	0.3	11.9[c]	1.3[d]	–	–
	HT					0.114[d]			0.88[d]		
Gasket (Flexitallic 866)	–	na	1−2e−3	–	–	0.019[e]	0	13.9	–	–	–
Metallic parts (Crofer22APU)	RT	0	0.5−2e−3	–	–	216	0.3	11.9[c]	248	–	–
	HT					71			35		

[a] Assumed values.

[b] 0.33 porosity.

[c] Value from RT to 1073 K. Temperature-dependent values implemented in the model.

[d] Computed from dense material.

[e] Through the thickness: Full non-linear pressure-closure relation.

Table 2
Fixed inlet conditions for the thermo-electrochemical cases.

	Partially prereformed methane	TPOx reformate
x_{H_2}	0.263	0.283
x_{H_2O}	0.493	0.060
x_{N_2}	0.000	0.489
x_{CH_4}	0.171	0.000
x_{CO}	0.029	0.125
x_{CO_2}	0.044	0.043
T_{AIR}	973.15	973.15
T_{FUEL}	973.15	973.15

chemical model was calibrated. The associated loss of accuracy has been underscored previously in Part I [24].

The history of a test is of main interest once plastic deformation is considered. The following sequence of structural analysis steps was computed for both co- and counter-flow configurations under both TPOX and internal steam–methane reforming conditions, leading to a set of 4 thermo-electrochemical cases:

- Assembly: sintering and cool-down to room temperature, assembly load at room temperature, heat-up and reduction at a uniform temperature of 1073 K. These steps are referred as INI1-4.
- IV: steady-state computation, gas flows fixed for the nominal operating point. The air ratio was set to ensure a maximum temperature in the SRU close to 1100 K. Six temperature profiles, ranging from open-circuit voltage (OCV) to the end of the current–voltage characterisation were imported into the finite-element tool. These steps are referred as IV1-6, IV5 corresponding to the nominal point (0.4 A cm^{-2}).
- Variation of electrical load: idle conditions (fuel flow: 1.4–3.5 nmlpm cm^{-2}, air ratio: 3–4), nominal load (0.275 W cm^{-2}), part load (0.175 W cm^{-2}), minimum load (0.1 W cm^{-2}), and back to nominal load. Gas flows and current density were controlled by PIDs, to achieve the fixed fuel utilisation (0.7–0.725), air outlet temperature (1100 K) and electrical

power, respectively. Nine temperature profiles from the dynamic simulations were selected depending on the value of the thermal gradients and temperature difference over the SRU and imported into the finite-element tool. These steps are referred as LS7-15.
- Rapid electrical load shutdown: OCV, fuel flow at minimum allowed value (1.5 nmlpm cm^{-2}), high air flow (100 nmlpm cm^{-2}) followed by a cool-down to room temperature. One typical temperature profile was selected during the load shutdown. The two last conditions are uniform temperatures of 673 and 298 K over the SRU. These steps are referred as SH16-18.

The inlet conditions that were fixed for all simulations are listed in Table 2. Table 3 lists the values of the current density and potential for steps IV1-LS15, whereas Table 4 provides the maximum thermal gradient and temperature difference for one analysis step per group in the 4 different thermo-electrochemical cases, i.e. co- and counter-flow configurations and with TPOX reformate or partially steam-reformed methane. Thus, analysis steps IV1-6, LS7-15 and SH16-18 refer to IV characterisation, dynamic variation of the electrical load and rapid load shutdown and cooldown, respectively.

All thermo-electrochemical cases in counter-flow configuration were simulated for the C1 cell with two different initial thicknesses of the gaskets, i.e. a value identical to, or 5% thicker than that of the GDL. They are identified as cases of gasket "no preload" and "preload", respectively. The latter is the default case. Thus, all simulations with the C2 cell included 5% thicker gaskets.

The evolution of the contact pressure was monitored at several locations during the analysis steps, e.g. symmetry line or fuel manifold. Analysis revealed the edge of the GDLs and SRU, namely locations A and B in Fig. 1 at either air inlet or outlet as subjected to the most important loss of contact pressure during operation. In addition, location B is significantly affected by the changes in curvature of the cell. Therefore, detailed results are presented only for these locations.

The assessment of the possible occurrence of thermal buckling of the MIC was performed for each thermo-electrochemical case: the

Table 3
Values of current density and voltage for steps IV1-LS15.

	TPOX reformate				Partially steam-reformed methane			
	Co-flow		Counter-flow		Co-flow		Counter-flow	
	U [V]	j [A cm^{-2}]	U [V]	j [A cm^{-2}]	U [V]	j [A cm^{-2}]	U [V]	j [A cm^{-2}]
IV1	1.00	0.00	1.00	0.00	0.97	0.00	0.99	0.00
IV2	0.89	0.10	0.89	0.10	0.81	0.10	0.89	0.10
IV3	0.82	0.20	0.82	0.20	0.77	0.20	0.84	0.20
IV4	0.76	0.30	0.77	0.30	0.75	0.30	0.81	0.30
IV5	0.67	0.40	0.69	0.40	0.73	0.40	0.77	0.40
IV6	0.62	0.42	0.66	0.42	0.71	0.44	0.75	0.44
LS7	0.82	0.23	0.87	0.15	0.79	0.05	0.74	0.37
LS8	0.74	0.38	0.75	0.37	0.65	0.42	0.78	0.36
LS9	0.71	0.39	0.75	0.37	0.75	0.37	0.82	0.34
LS10	0.70	0.40	0.72	0.38	0.79	0.35	0.84	0.21
LS11	0.79	0.22	0.80	0.22	0.79	0.35	0.84	0.21
LS12	0.84	0.12	0.85	0.12	0.83	0.21	0.86	0.18
LS13	0.78	0.29	0.81	0.22	0.86	0.12	0.87	0.12
LS14	0.72	0.38	0.72	0.38	0.80	0.35	0.82	0.34
LS15	0.70	0.40	0.72	0.39	0.76	0.36	0.81	0.34

Table 4
Representative values for each group of analysis steps of the structural analysis.

Analysis step	TPOX reformate						Partially steam-reformed methane					
	Co-flow			Counter-flow			Co-flow			Counter-flow		
	IV5	LS8	SH16	IV5	LS8	SH16	IV5	LS8	SH16	IV5	LS8	SH16
Max. local current density [A cm^{-2}]	0.56	0.60	–	0.81	0.68	–	0.56	0.68	–	0.75	0.48	–
Max. thermal gradient [K m^{-1}]	1988	3221	805	1548	2062	812	1948	1743	1030	1239	2332	711
Max. temperature difference [K]	126	163	105	132	173	95	144	130	105	109	120	78

thickness for the calculation of the temperature profile was kept at a constant value of 2.5 mm, while it was varied in the finite-element tool from 0.8 to 1.8 mm in increments of 0.1 mm, until no buckling of the MIC was observed after the release of the load.

3. Results and discussion

3.1. Thermal buckling of the metallic interconnector

The computed temperature profiles display large temperature differences and zones of relatively higher temperature as depicted in Fig. 3. Thermal buckling of the MIC, for instance, can arise in such conditions. Fig. 4 compiles the results of the computed minimum stable MIC thickness for the 3 different groups of analysis steps in the thermo-electrochemical cases. It should be emphasised that the minimum stable MIC thickness is expected to be yet slightly higher in reality, since the applied temperature profiles were all generated from thermo-electrochemical simulations with a thickness of 2.5 mm. Thicker MICs induce an increase of the effective in-plane thermal conductivity of the solid and consequently tend to flatten the temperature profile.

Operation with TPOX reformate is less critical than internal steam–methane reforming. The same holds for counter with respect to co-flow configuration, at the end of the current–voltage characterisation. Actually, the MIC is less prone to thermal buckling in the co-flow configuration in the nominal range, i.e. at current densities lower than $0.4\,A\,cm^{-2}$ (IV5). This change is caused by the lower performance of the co-flow configuration. An increase of the air flow would be required to maintain an identical air outlet temperature among the thermo-electrochemical cases above the nominal operating point (IV5). All critical cases occur during transient operation, where higher thermal gradients and local increase of the temperature can arise (cf. Table 4). However, there is not necessarily a correlation between the risks of buckling and cell fracture (Part I [24]): the rapid load shutdown procedure (SH16), which did not induce particular harmful conditions for the cell in both co- and counter-flow configurations appears as the most critical case in term of risk of thermal buckling for the co-flow configuration, when the SRU is fed with TPOX reformate.

The occurrence of thermal buckling can be acceptable if it does not provoke large displacements or plastic deformation. Fig. 5 depicts the temperature profile and the associated MIC vertical displacement along the symmetry line of the repeat element along the gas flows for the most critical operating conditions and a MIC thickness of 1.2 mm. The maximum computed displacements are larger than the thickness of the GDL on the anode side in almost all cases. Such conditions are likely to cause the malfunction of the sealing system and damage to the compliant metallic foam used here as GDL, which are harmful conditions for the stack integrity. In the worst case, redistribution of the gas flows, due to a local decrease of porosity of the plastically deformed foam can be expected. Such a phenomenon is difficult to control, but the dissymmetry in the corrosion scales, e.g. air and fuel side and small pressure differences might be sufficient to force the buckling to occur in the same direction in all repeat elements of a stack. In addition, the yield stress of the MIC material is very low at high temperature [15]: the convex side can undergo plastic deformation, which will then influence the behaviour during subsequent steps. Therefore designing a stack without preventing the occurrence of buckling appears as a very ambitious task at the current level of knowledge. An increase of the thickness of the critical components is the straightforward countermeasure. Unfortunately, it implies an increase of the weight and of the thermal inertia of the stack, which affects its ability to comply with any application where fast heat-up or cool-down are required. This is currently a key issue in SOFC.

A relatively simple indicator, such as the maximum thermal gradient or the maximum temperature difference over the SRU, would be of the highest interest during both the design and service phase of the life of a SOFC stack. In the first case, it can assist the selection of proper materials and test different geometries, depending on the requirement. In the second case, it can be implemented in a control strategy, if the indicator is simple to measure in a stack. Unfortunately, as for the assessment of cell failure [24], a simple and reliable relation could not be established between the risk of buckling and thermal gradients nor temperature difference, as shown in Fig. 6.

3.2. Loss of contact pressure on the gaskets

Gas-tightness and electrical contact are conditions for the proper operation of a stack. It is well confirmed from short-stack experiments that both defaults usually lead to a premature failure of the stack. Indeed, gas leaks have plethora of critical effects, which range from loss of performance due to the leak to local reoxidation of the anode or reduction of the cathode material [1].

Fig. 3 provides a qualitative overview of the phenomena. The contact pressure is plotted for the most critical analysis steps (LS8 and LS9) in term of loss of contact pressure at location B, at the air outlet. The comparison between the temperature profiles at the nominal (IV5) and most critical conditions (LS8 and LS9) (middle and right columns) highlights how a zone of relatively higher temperature, located in the area of highest local current density can develop during transient operation. The position of the maximum contact pressure can be obviously determined from the observation of the temperature profile. It is the highest on the GDL (highest local temperature), whereas a decrease occurs on the gaskets, at the edge of the SRU (location B) at the air outlet. The extension of this zone of lower contact pressure towards the fuel manifold is more or less pronounced and affects either the fuel inlet or outlet manifold in counter- and co-flow, respectively. Therefore, co- and counter-flow configurations are expected to present a different resistance towards the release of contact pressure at the air outlet, in favor of the former since the decrease occurs at the fuel outlet, while the inlet area is submitted to higher compressive stresses.

Fig. 7 depicts the evolution of the distribution of the contact pressure on the fuel GDL along the central axis of symmetry, with and without gasket preload, during the variation of the electrical load, when the SRU is operated in counter-flow configuration and fed with partially steam-reformed methane. The level of stress is high for metallic foam in a high-temperature environment and induces plastic deformation. In addition, the variations during the different analysis steps are significant. History-dependent behaviours were thus expected, but the simulations indicate that electrical contact is ensured over the whole active area independently of the analysis, even though loss of contact is observed at the frontier between the gasket and the GDL. The affected area remains very narrow and is not believed to induce a noticeable change of the imported temperature profile.

The requirement is different for the gasket, since a compressive stress, instead of simple contact has to be ensured during service at all time. Fig. 8 depicts the evolution of the pressure versus closure during the different analysis steps at 3 different locations of the air gasket, namely (i) A, air outlet, (ii) B, air inlet and (iii) B, air outlet, which can be identified in Fig. 1. A C1 cell is used, the SRU is operated in counter-flow configuration, fed with TPOX reformate. The gasket is preloaded. The evolution among the different analysis steps is as follows:

- Assembly (grey lines and crosses): the contact pressure is locally the highest at room temperature, after the assembly step. The uneven distribution between locations A and B is due to the cell curvature.
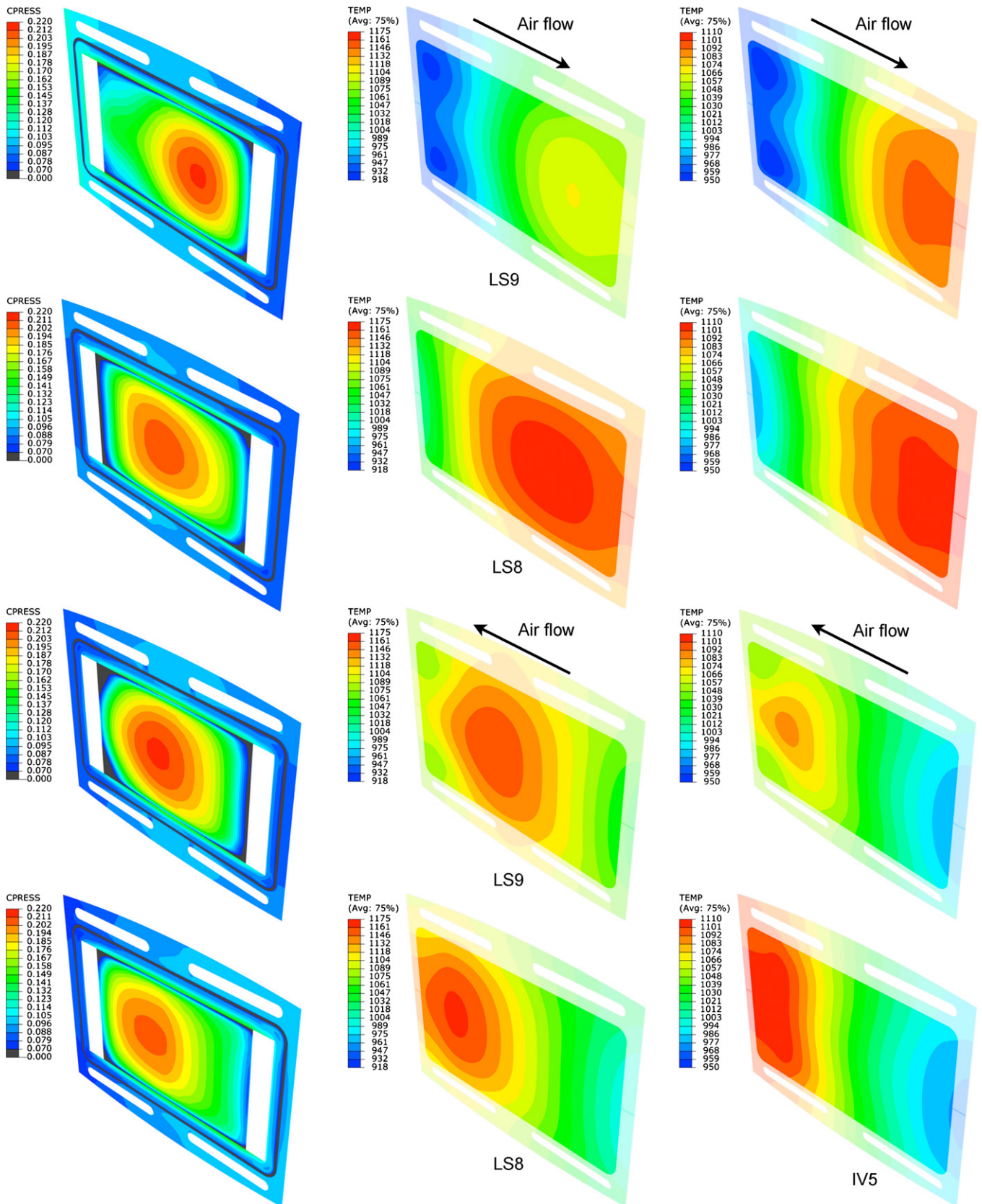
Fig. 3. Contact pressure [MPa] on the GDL and gaskets on the fuel side (left) and corresponding temperature (middle) for the most critical analysis steps (LS8 and LS9), in term of loss of contact pressure at the edge of the SRU (location B). Case of gasket preload. The temperature profile at nominal point (IV5) is depicted for comparison (right). Internal steam–methane reforming, co-flow configuration (top), TPOX, co-flow configuration (second), internal steam–methane reforming, counter-flow configuration (third), TPOX, counter-flow configuration (bottom).
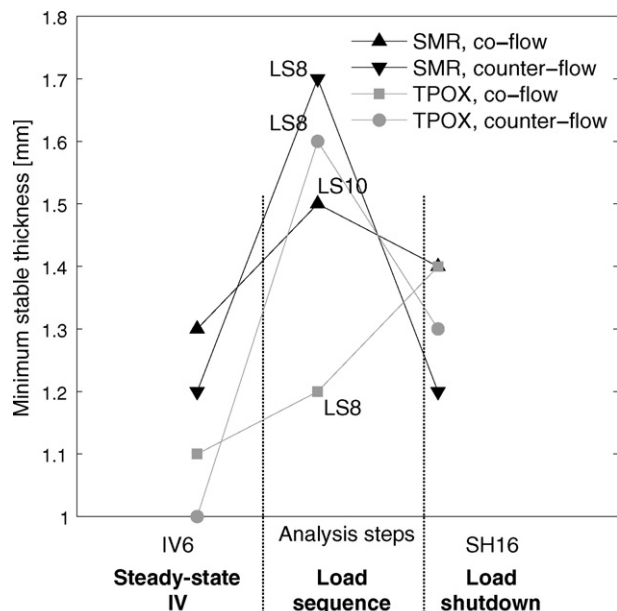
Fig. 4. Minimum computed stable thickness of the metallic interconnector for the 4 different thermo-electrochemical cases.

- Uniform heating (grey lines and crosses): the contact pressure remains almost similar at the edge of the SRU (B). The temperature increase reduces the residual stresses in the cell and thus the curvature. Hence a more pronounced decrease of the contact pressure is observed at the edge of the GDL (A).
- Current–voltage characterisation (black squares): the contact pressure decreases at the edge of both the SRU (B) and GDL (A) at the air outlet, due to development of the zone of relatively higher temperature located in the active area. The situation is the opposite at the edge of the SRU (B), at the air inlet, due to the cooling of the entering air (Fig. 3). Rotation of the MIC around the *y*-axis (Fig. 1) is allowed and it therefore touches preferentially the areas of locally highest temperature, as is qualitative best depicted in Fig. 3. The contact pressure at the end of the IV characterisation is higher than at room temperature and an increment of plastic strain is generated (insert in Fig. 8). Hence, after a thermal cycle, a
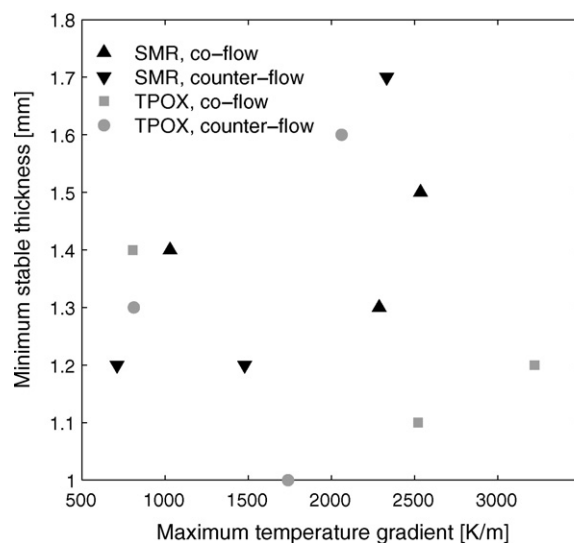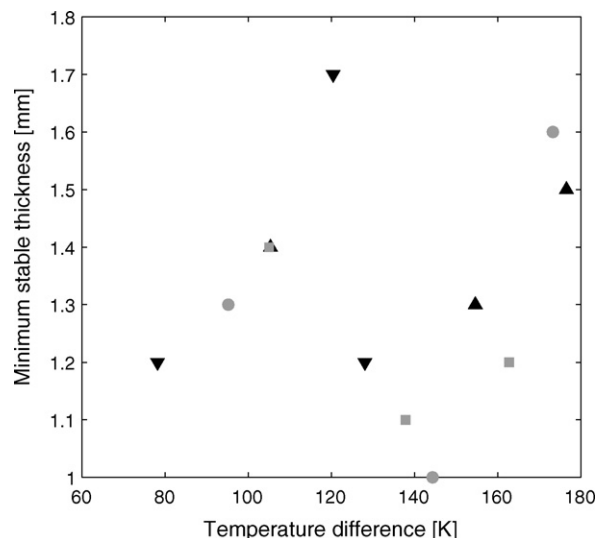
Fig. 6. Correlation between minimum stable MIC thickness to prevent any thermal buckling and temperature difference (top) and maximum thermal gradient (bottom) over the SRU.
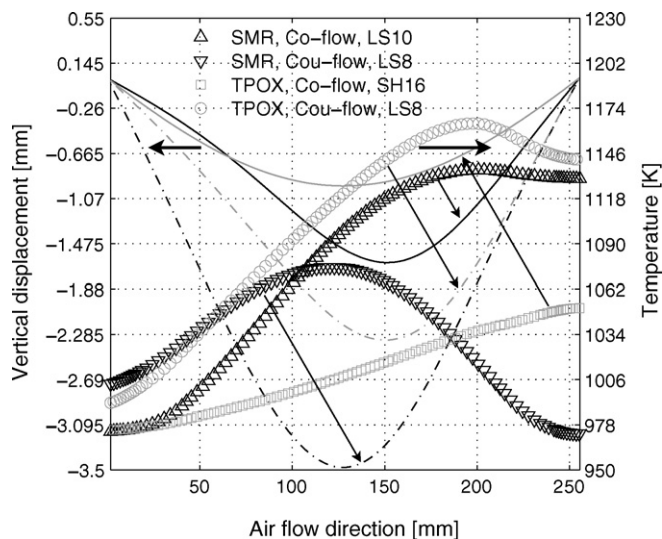

Fig. 5. Temperature profiles and associated vertical displacement during thermal buckling along the symmetry line for the most critical analysis steps during the IV characterisation, the variation of the electrical load and rapid electrical load shutdown. Thickness of the MIC of 1.2 mm.
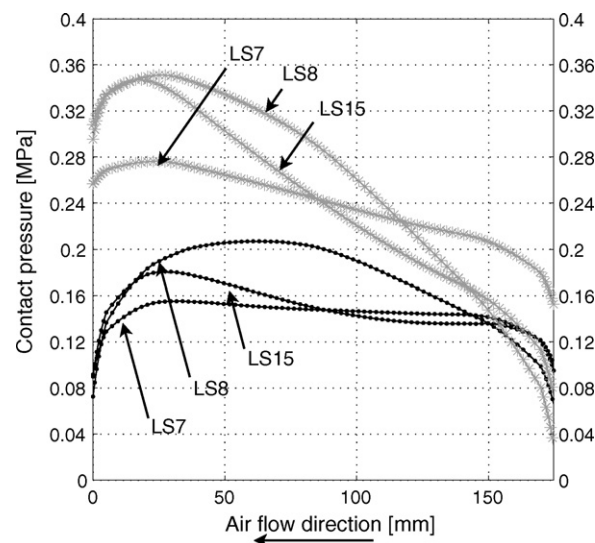

Fig. 7. Contact pressure on the gas diffusion layer with (black) or without (grey) initial preload on the gaskets. C1 cell, partially steam-reformed methane, counter-flow.
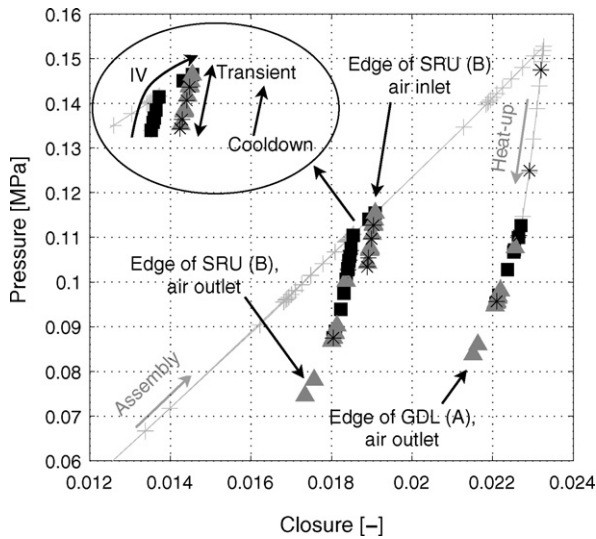
Fig. 8. Details of the evolution of the pressure versus closure. C1 cell, TPOX reformate and counter-flow configuration. Locations A and B refer to Fig. 1. Assembly and heat-up (grey crosses), current–voltage characterisation (black squares), variation of the electrical load (grey triangles) and load shutdown and cooldown (black stars).
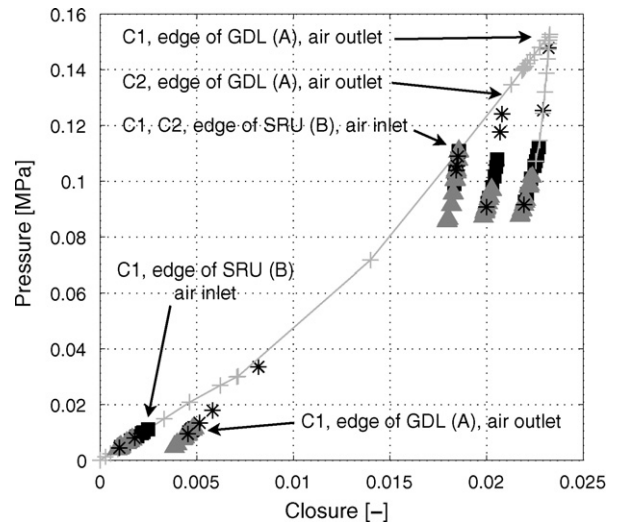

Fig. 9. Evolution of the pressure versus closure with (higher contact pressure, upper right group) or without (lower contact pressure, lower left group) initial preload on the gaskets, for the C1 and C2 cell. Assembly and heat-up (grey crosses), current–voltage characterisation (black squares), variation of the electrical load (grey triangles) and load shutdown and cooldown (black stars). Partially steam-reformed methane, counter-flow configuration. Locations A and B refer to Fig. 1.

permanent increment of plastic strain at location B is generated. Thus the state of the gasket at room temperature after a thermal cycle can be altered, depending on the operating sequence.

- Variation of the electrical load (grey triangles): the contact pressure varies depending on the shape of the temperature profile. The decrease can significantly extend to the fuel manifold. A change in unloading path is observed at the edge of the SRU, at the air inlet, due to the increment of plastic strain generated at the end of the IV characterisation.
- Rapid load shutdown and cooldown (black crosses): the contact pressure increases again.

The trends were similar when the SRU was fed with partially steam-reformed methane, except that no increment of plastic strain was observed at the air inlet, due to the lower required air ratio.

Fig. 9 displays the influence of the gasket preload and types of cell. A significant variation is observed. Unlike the gasket-preloaded situation depicted in Fig. 3, the GDL takes most of the assembly load and therefore releases the gaskets, when no preload is applied on the latter (Fig. 7). In this case, the loss of pressure on the gasket is almost complete at the 3 locations. The effect of the preload on the gaskets is therefore beneficial, since it uniformises the contact pressure over the SRU. Nevertheless, strong decreases during operation cannot be prevented and a drop in contact pressure as high as 40%, compared to the state at room temperature, is observed depending on the location. It should be emphasised that the above-mentioned comments do not necessarily hold for any selection of materials, since either loss of gas-tightness or electrical contact can occur, depending on the material properties, which will influence the component that withstands most of the assembly load.

Finally, the effect of the cell curvature due to residual stresses on the contact pressure at the edge of the GDL is observed in Fig. 9: this phenomenon is less pronounced for the C2 cell at room temperature, due to the compensating layer. In comparison, the edges of the SRU are not significantly affected, since the cell does not extend up to this location.

3.3. Plastic deformation in the metallic interconnect

The evolution of the maximum von Mises stress in the MIC and the occurrence and incremental increase of the equivalent plastic

strain is depicted in Fig. 10. The occurrence of plastic strain and maximum probability of failure of the cell (see Fig. 6 of Part I [24]) do not appear at the same operating points. The highest plastic strains are generated during the cool-down in the counter-flow configuration and when the SRU is fed with partially steam-reformed methane. Plastic strain is not directly related to highest stresses, since the yield stress of the MIC material strongly depends on the temperature. The plastic deformation (i) induces remaining stresses around 72.7–82.1 MPa, which correspond to a value of 0.29–0.33, relative to the 0.2% yield strength of the MIC material at room temperature, and localised in narrow areas near the fuel manifold at room temperature and (ii) a slightly different stress profile in the gasket compared to the assembly step, due to the friction. The associated risks could not be assessed, since a failure criterion could not be found for the gasket material. Nevertheless, the influ-
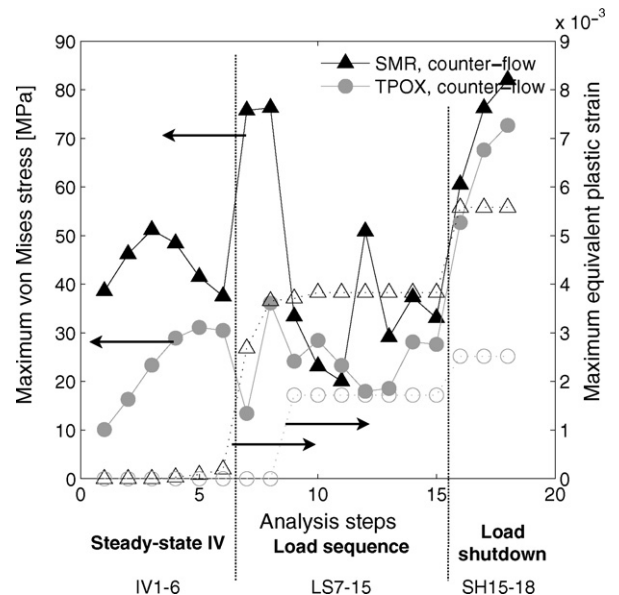

Fig. 10. Evolution of the maximum equivalent plastic strain and von Mises stress in the metallic interconnector during the different analysis steps. C1 cell.

ence on cell probability of failure is negligible (see Fig. 5 of Part I [24]).

4. Conclusion

Coupling a detailed thermo-electrochemical model to a finite-element tool enabled the structural analysis of the SOFC stack of latest generation developed within the frame of the FLAMESOFC stack at LENI-EPFL in collaboration with SOFCPower and HTceramix. All components of a single representative repeat unit were meshed and their interactions modelled through contact simulations.

Simple computations on a dedicated model showed that buckling of the MIC appears as a likely and possibly harmful phenomenon in SOFC stacks and prevents at the current state of knowledge any unconsidered decrease of the MIC thickness to reduce the weight and thermal inertia. Relations between the risk of buckling of the MIC and maximum thermal gradient or temperature difference over the SRU could not be established. Similarly, the most critical situations in terms of thermal buckling do not correspond to the one for cell fracture, which were computed in Part I.

Simulations showed that contact pressure on the GDL, hence electrical contact was ensured during the whole analysis, even though plastic strain was generated. On the other hand, a large decrease of contact pressure was observed in the gasket. Critically affected areas include the fuel manifold on the air outlet side: the resistance of co- or counter-flow configurations towards such phenomena is expected to differ. Almost complete release occurred at particular locations when no preload was applied on the gaskets. The temperature profile and/or the residual stresses in the cell were revealed as the causes for the observed behaviour, depending on the location.

Acknowledgements

References

[1] Z. Wuillemin, N. Autissier, A. Nakajo, M.-T. Luong, J. Van Herle, D. Favrat, Fuel Cell Science and Technology 5 (1) (2008) 011016–011019.

[2] D. Sarantaridis, R.A. Rudkin, A. Atkinson, Journal of Power Sources 180 (2008) 704–710.

[3] H. Yakabe, I. Yasuda, Journal of The Electrochemical Society 150 (1) (2003) A35–A43.

[4] H. Yakabe, T. Ogiwara, M. Hishinuma, I. Yasuda, Journal of Power Sources 102 (2001) 144–154.

[5] H. Yakabe, Y. Baba, T. Sakurai, Journal of Power Sources 135 (2004) 9–16.

[6] H. Yakabe, Y. Baba, T. Sakurai, Journal of Power Sources 131 (2004) 278–284.

[7] A. Selimovic, M. Kemm, T. Torisson, M. Assadi, Journal of Power Sources 145 (2005) 463–469.

[8] C.-K. Lin, T.-T. Chen, Y.-P. Chyou, L.-K. Chiang, Journal of Power Sources 164 (2007) 238–251.

[9] A. Nakajo, C. Stiller, G. Härkegard, O. Bolland, Journal of Power Sources 158 (2006) 287–294.

[10] A. Atkinson, A. Selçuk, Acta Materialia 47 (3) (1999) 867–874.

[11] A. Atkinson, A. Selçuk, Solid State Ionics 134 (2000) 59–66.

[12] M. Radovic, E. Lara-Curzio, Acta Materialia 52 (2004) 5747–5756.

[13] D.L. Meixner, R.A. Cutler, Solid State Ionics 146 (2002) 285–300.

[14] Y.S. Chou, J.W. Stevenson, T.R. Armstrong, L.R. Pederson, Journal of the American Ceramic Society 83 (6) (2000) 1457–1464.

[15] ThyssenKrupp VDM, Material Data Sheet No. 4046, http://thyssenkruppvdm. de/_pdf/Crofer22APU_e.pdf.

[16] L.J. Gibson, M.F. Ashby, Cellular Solids: Structure & Properties, Pergamon Press, New York, 1988.

[17] M. Bram, S. Reckers, P. Drinovac, J. Mönch, R.W. Steinbrech, H.P. Buchkremer, D. Stöver, Journal of Power Sources 138 (2004) 111–119.

[18] A.-H. Bouzid, H. Champliaud, Journal of Pressure Vessel Technology 126 (2004) 445–450.

[19] R. Goodall, C. Williams, J.A. Fernie, T.W. Clyne, et al., Thermal expansion and stiffness characteristics of a highly porous, fire-resistant composite material, International SAMPE Symposium and Exhibition (Proceedings) 47 II 1001–1010.

[20] S.H. Chan, X.J. Chen, K.A. Khor, Journal of The Electrochemical Society 151 (1) (2004) A164–A172.

[21] P. Costamagna, P. Costa, V. Antonucci, Electrochimica Acta 43 (1998) 375–394.

[22] B. Kenney, K. Karan, Solid State Ionics 178 (2007) 297–306.

[23] C. Stiller, B. Thorud, O. Bolland, R. Kandepu, L. Imsland, Journal of Power Sources 158 (2006) 303–315.

[24] A. Nakajo, Z. Wuillemin, J. Van herle, Journal of Power Sources 193 (2009) 203–215.

[25] D. Larrain, J. Van herle, F. Maréchal, D. Favrat, Journal of Power Sources 131 (2004) 304–312.

[26] gPROMS (General Process Modelling and Simulation Tool), v3.0.2, Process Systems Enterprise Ltd, London, http://www.psenterprise.com/.

[27] C. Stiller, B. Thorud, S. Seljebø, Ø. Mathisen, H. Karoliussen, O. Bolland, Journal of Power Sources 141 (2005) 227–240.

[28] J.H. Park, R.N. Blumenthal, Journal of The Electrochemical Society 136 (1989) 2867.

[29] J. Fleig, H.L. Tuller, J. Maier, Solid State Ionics 174 (2004) 261–270.

[30] R.J. Kee, H. Zhu, Journal of Power Sources 117 (2003) 61–74.

[31] E. Achenbach, E. Riensche, Journal of Power Sources 52 (1994) 283–288.

[32] W.G. Bessler, Journal of The Electrochemical Society 153 (8) (2006) A1492–A1504.

[33] F.H. van Heuvel, H.J.M. Bouwmeester, Journal of The Electrochemical Society 144 (1) (1997).

[34] ABAQUS Inc., v6.7, Hibbitt, Karlsson and Sorensen, Rhode Island.

[35] MATLAB, v7.5, The Mathworks Inc., Natik.

[36] A.C. Müller, A. Krügel, A. Weber, E. Ivers-Tiffée, Materials Research Society Symposium - Proceedings 756 (2003) 533–538.

[37] J. Laurencin, G. Delette, F. Lefebvre-Joud, M. Dupeux, Journal of the European Ceramic Society 28 (9) (2008) 1857–1869.

[38] A. Selçuk, A. Atkinson, Journal of the European Ceramic Society 17 (1997) 1523–1532.

[39] M. Mori, Solid State Ionics 174 (2004) 1–8.

[40] N.Q. Minh, T. Takahashi, Science and Technology of Ceramic Fuel Cells, Elsevier, 1995.

[41] ThyssenKrupp VDM, Material Data Sheet No. 1001, www.thyssenkrupp-vdm-fareast.com/media/down_datasheets_corres_new/nickel_99_2_e.pdf.